

1 **Large-scale, high-resolution comparison of the core visual object  
2 recognition behavior of humans, monkeys, and state-of-the-art deep  
3 artificial neural networks**

4  
5 Abbreviated title: Comparing object recognition between primates and models  
6

7 Rishi Rajalingham\*, Elias B. Issa\*, Pouya Bashivan, Kohitij Kar, Kailyn Schmidt, and James J.  
8 DiCarlo  
9

10 McGovern Institute for Brain Research and Department of Brain and Cognitive Sciences  
11 Massachusetts Institute of Technology, Cambridge, Massachusetts 02139  
12

13 \*R.R. and E.B.I. contributed equally to this work.  
14

15 Correspondence should be addressed to James J. DiCarlo, McGovern Institute for Brain  
16 Research, Department of Brain and Cognitive Sciences, Massachusetts Institute of Technology,  
17 77 Massachusetts Institute of Technology, 46-6161, Cambridge, MA 02139. E-mail:  
18 [dicarlo@mit.edu](mailto:dicarlo@mit.edu)  
19

20 E. Issa's present address: Department of Neuroscience, Zuckerman Mind Brain Behavior  
21 Institute, Columbia University, New York, NY 10027  
22

---

23 Targeting *Journal of Neuroscience*  
24

25 Title 19 words  
26

27 Abbreviated Title 50 characters  
28

29 Abstract 242 words  
30

31 Significance Statement 97 words  
32

33 Introduction 649 words  
34

35 Discussion 1188 words  
36

37 Figures 6  
38

39 \*All word limits include citations  
40

---

41 **AUTHOR CONTRIBUTIONS**  
42

43 E.B.I., R.R., and J.J.D designed the experiments. E.B.I., K.S., R.R., and K.K. carried out the  
44 experiments. R.R., E.B.I., and P.B. performed the data analysis and modeling. R.R., E.B.I., and  
45 J.J.D. wrote the manuscript.  
46

47 **ACKNOWLEDGEMENTS**  
48

49 This research was supported by US National Eye Institute grants R01-EY014970 (J.J.D.) and  
50 K99-EY022671 (E.B.I.), Office of Naval Research MURI-114407 (J.J.D.), IARPA Contract  
51 D16PC00002 (J.J.D), Engineering Research Council of Canada (R.R.), and The McGovern  
52 Institute for Brain Research  
53

54 **COMPETING FINANCIAL INTERESTS**  
55

56 The authors declare no competing financial interests.  
57

47 **ABSTRACT**

48

49       Primates—including humans—can typically recognize objects in visual images at a  
50       glance even in the face of naturally occurring identity-preserving image transformations (e.g.  
51       changes in viewpoint). A primary neuroscience goal is to uncover neuron-level mechanistic  
52       models that quantitatively explain this behavior by predicting primate performance for each and  
53       every image. Here, we applied this stringent behavioral prediction test to the leading mechanistic  
54       models of primate vision (specifically, deep, convolutional, artificial neural networks; ANNs) by  
55       directly comparing their behavioral signatures against those of humans and rhesus macaque  
56       monkeys. Using high-throughput data collection systems for human and monkey psychophysics,  
57       we collected over one million behavioral trials for 2400 images over 276 binary object  
58       discrimination tasks. Consistent with previous work, we observed that state-of-the-art deep, feed-  
59       forward convolutional ANNs trained for visual categorization (termed DCNN<sub>IC</sub> models)  
60       accurately predicted primate patterns of object-level confusion. However, when we examined  
61       behavioral performance for individual images within each object discrimination task, we found  
62       that all tested DCNN<sub>IC</sub> models were significantly non-predictive of primate performance, and  
63       that this prediction failure was not accounted for by simple image attributes, nor rescued by  
64       simple model modifications. These results show that current DCNN<sub>IC</sub> models cannot account for  
65       the image-level behavioral patterns of primates, and that new ANN models are needed to more  
66       precisely capture the neural mechanisms underlying primate object vision. To this end, large-  
67       scale, high-resolution primate behavioral benchmarks—such as those obtained here—could serve  
68       as direct guides for discovering such models.

69

70

71 **SIGNIFICANCE STATEMENT**

72

73 Recently, specific feed-forward deep convolutional artificial neural networks (ANNs)  
74 models have dramatically advanced our quantitative understanding of the neural mechanisms  
75 underlying primate core object recognition. In this work, we tested the limits of those ANNs by  
76 systematically comparing the behavioral responses of these models with the behavioral responses  
77 of humans and monkeys, at the resolution of individual images. Using these high-resolution  
78 metrics, we found that all tested ANN models significantly diverged from primate behavior.  
79 Going forward, these high-resolution, large-scale primate behavioral benchmarks could serve as  
80 direct guides for discovering better ANN models of the primate visual system.

81

82 **INTRODUCTION**

83

84       Primates—both human and non-human—can typically recognize objects in visual images  
85 at a glance, even in the face of naturally occurring identity-preserving transformations such as  
86 changes in viewpoint. This view-invariant visual object recognition ability is thought to be  
87 supported primarily by the primate ventral visual stream (DiCarlo et al., 2012). A primary  
88 neuroscience goal is to construct computational models that quantitatively explain the neural  
89 mechanisms underlying this ability. That is, our goal is to discover artificial neural networks  
90 (ANNs) that accurately predict neuronal firing rate responses at all levels of the ventral stream  
91 and its behavioral output. To this end, specific models within a large family of deep,  
92 convolutional neural networks (DCNNs), optimized by supervised training on large-scale  
93 category-labeled image-sets (ImageNet) to match human-level categorization performance  
94 (Krizhevsky et al., 2012; LeCun et al., 2015), have been put forth as the leading ANN models of  
95 the ventral stream (Yamins and DiCarlo, 2016). We refer to this sub-family as DCNN<sub>IC</sub> models  
96 (IC to denote ImageNet-categorization pre-training), so as to distinguish them from all possible  
97 models in the DCNN family, and more broadly, from the super-family of all ANNs. To date, it  
98 has been shown that DCNN<sub>IC</sub> models display internal feature representations similar to neuronal  
99 representations along the primate ventral visual stream (Yamins et al., 2013; Cadieu et al., 2014;  
100 Khaligh-Razavi and Kriegeskorte, 2014; Yamins et al., 2014), and they exhibit behavioral  
101 patterns similar to the behavioral patterns of pairwise object confusions of primates  
102 (Rajalingham et al., 2015). Thus, DCNN<sub>IC</sub> models may provide a quantitative account of the  
103 neural mechanisms underlying primate core object recognition behavior.

104

105       However, several studies have shown that DCNN<sub>IC</sub> models can diverge drastically from  
106 humans in object recognition behavior, especially with regards to particular images optimized to  
107 be adversarial to these networks (Goodfellow et al., 2014; Nguyen et al., 2015). Related work  
108 has shown that specific image distortions are disproportionately challenging to current DCNNs,  
109 as compared to humans (RichardWebster et al., 2016; Dodge and Karam, 2017; Geirhos et al.,  
110 2017; Hosseini et al., 2017). Such image-specific failures of the current ANN models would  
111 likely not be captured by “object-level” behavioral metrics (e.g. the pattern of pairwise object  
112 confusions mentioned above) that are computed by pooling over hundreds of images and thus are

113 not sensitive to variation in difficulty across images of the same object. To overcome this  
114 limitation of prior work, we here aimed to use scalable behavioral testing methods to precisely  
115 characterize primate behavior at the resolution of individual images and to directly compare  
116 leading DCNN models to primates over the domain of core object recognition behavior at this  
117 high resolution.

118

119 We focused on *core invariant object recognition*—the ability to identify objects in visual  
120 images in the central visual field during a single, natural viewing fixation (DiCarlo et al., 2012).  
121 We further restricted our behavioral domain to *basic-level* object discriminations, as defined  
122 previously (Rosch et al., 1976). Within this domain, we collected large-scale, high-resolution  
123 measurements of human and monkey behavior (over a million behavioral trials) using high-  
124 throughput psychophysical techniques—including a novel home-cage behavioral system for  
125 monkeys. These data enabled us to systematically compare all systems at progressively higher  
126 resolution. At lower resolutions, we replicated previous findings that humans, monkeys, and  
127 DCNN<sub>IC</sub> models all share a common pattern of object-level confusion (Rajalingham et al., 2015).  
128 However, at the higher resolution of individual images, we found that the behavior of all tested  
129 DCNN<sub>IC</sub> models was significantly different from human and monkey behavior, and this model  
130 prediction failure could not be easily rescued by simple model modifications. These results show  
131 that current DCNN<sub>IC</sub> models do not fully account for the image-level behavioral patterns of  
132 primates, suggesting that new ANN models are needed to more precisely capture the neural  
133 mechanisms underlying primate object vision. To this end, large-scale high-resolution behavioral  
134 benchmarks, such as those obtained here, could serve as a strong top-down constraint for  
135 efficiently discovering such models.

136

137

## 138 MATERIALS & METHODS

139

### 140 *Visual images*

141 We examined basic-level, core object recognition behavior using a set of 24 broadly-  
142 sampled objects that we previously found to be reliably labeled by independent human subjects,  
143 based on the definition of basic-level proposed by (Rosch et al., 1976). For each object, we

144 generated 100 naturalistic synthetic images by first rendering a 3D model of the object with  
145 randomly chosen viewing parameters (2D position, 3D rotation and viewing distance), and then  
146 placing that foreground object view onto a randomly chosen, natural image background. To do  
147 this, each object was first assigned a canonical position (center of gaze), scale (~2 degrees) and  
148 pose, and then its viewing parameters were randomly sampled uniformly from the following  
149 ranges for object translation ([-3,3] degrees in both h and v), rotation ([-180,180] degrees in all  
150 three axes) and scale ([x0.7, x1.7]. Background images were sampled randomly from a large  
151 database of high-dynamic range images of indoor and outdoor scenes obtained from Dosch  
152 Design ([www.doschdesign.com](http://www.doschdesign.com)). This image generation procedure enforces invariant object  
153 recognition, rather than image matching, as it requires the visual recognition system (human,  
154 animal or model) to tackle the “invariance problem,” the computational crux of object  
155 recognition (Ullman and Humphreys, 1996; Pinto et al., 2008). Using this procedure, we  
156 previously generated 2400 images (100 images per object) rendered at 1024x1024 pixel  
157 resolution with 256-level gray scale and subsequently resized to 256x256 pixel resolution for  
158 human psychophysics, monkey psychophysics and model evaluation (Rajalingham et al., 2015).  
159 In the current work, we focused our analyses on a randomly subsampled, and then fixed, sub-set  
160 of 240 images (10 images per object; here referred to as the “primary test images”). Figure 1A  
161 shows the full list of 24 objects, with two example images of each object.  
162

163 Because all of the images were generated from synthetic 3D object models, we had  
164 explicit knowledge of the viewpoint parameters (position, size, and pose) for each object in each  
165 image, as well as perfect segmentation masks. Taking advantage of this feature, we characterized  
166 each image based on these high-level attributes, consisting of size, eccentricity, relative pose and  
167 contrast of the object in the image. The size and eccentricity of the object in each image were  
168 computed directly from the corresponding viewpoint parameters, under the assumption that the  
169 entire image would subtend 6° at the center of visual gaze (+/-3° in both azimuth and elevation;  
170 see below). For each synthetic object, we first defined its “canonical” 3D pose vector, based on  
171 independent human judgments. To compute the relative pose attribute of each image, we  
172 estimated the difference between the object’s 3D pose and its canonical 3D pose. Pose  
173 differences were computed as distances in unit quaternion representations: the 3D pose ( $r_{xy}$ ,  $r_{xz}$ ,  
174  $r_{yz}$ ) was first converted into unit quaternions, and distances between quaternions  $q_1$ ,  $q_2$  were

175 estimated as  $\cos^{-1}|q_1 \cdot q_2|$  (Huynh, 2009). To compute the object contrast, we measured the  
176 absolute difference between the mean of the pixel intensities corresponding to the object and the  
177 mean of the background pixel intensities in the vicinity of the object (specifically, within 25  
178 pixels of any object pixel, analogous to computing the local foreground-background luminance  
179 difference of a foreground object in an image). Figure 5C shows example images with varying  
180 values for the four image attributes.

181

### 182 *Core object recognition behavioral paradigm*

183 Core object discrimination is defined as the ability to discriminate between two or more  
184 objects in visual images presented under high view uncertainty in the central visual field (~10°),  
185 for durations that approximate the typical primate, free-viewing fixation duration (~200 ms)  
186 (DiCarlo and Cox, 2007; DiCarlo et al., 2012). As in our previous work (Rajalingham et al.,  
187 2015), the behavioral task paradigm consisted of a interleaved set of binary discrimination tasks.  
188 Each binary discrimination task is an object discrimination task between a pair of objects (e.g.  
189 elephant vs. bear). Each such binary task is balanced in that the test image is equally likely  
190 (50%) to be of either of the two objects. On each trial, a test image is presented, followed by a  
191 choice screen showing canonical views of the two possible objects (the object that was not  
192 displayed in the test image is referred to as the “distractor” object, but note that objects are  
193 equally likely to be distractors and targets). Here, 24 objects were tested, which resulted in 276  
194 binary object discrimination tasks. To neutralize feature attention, these 276 tasks are randomly  
195 interleaved (trial by trial), and the global task is referred to as a basic-level, core object  
196 recognition task paradigm.

197

### 198 *Testing human behavior*

199 All human behavioral data presented here were collected from 1476 human subjects on  
200 Amazon Mechanical Turk (MTurk) performing the task paradigm described above. Subjects  
201 were instructed to report the identity of the foreground object in each presented image from  
202 among the two objects presented on the choice screen (Fig 1B). Because all 276 tasks were  
203 interleaved randomly (trial-by-trial), subjects could not deploy feature attentional strategies  
204 specific to each object or specific to each binary task to process each test image.

205

206       Figure 1B illustrates the time course of each behavioral trial, for a particular object  
207 discrimination task (zebra versus dog). Each trial initiated with a central black point for 500 ms,  
208 followed by 100 ms presentation of a test image containing one foreground object presented  
209 under high variation in viewing parameters and overlaid on a random background, as described  
210 above (see *Visual images* above). Immediately after extinction of the test image, two choice  
211 images, each displaying a single object in a canonical view with no background, were shown to  
212 the left and right. One of these two objects was always the same as the object that generated the  
213 test image (i.e., the correct object choice), and the location of the correct object (left or right) was  
214 randomly chosen on each trial. After clicking on one of the choice images, the subject was  
215 queued with another fixation point before the next test image appeared. No feedback was given;  
216 human subjects were never explicitly trained on the tasks. Under assumptions of typical  
217 computer ergonomics, we estimate that images were presented at 6–8° of visual angle at the  
218 center of gaze, and the choice object images were presented at ±6–8° of eccentricity along the  
219 horizontal meridian.

220

221       We measured human behavior using the online Amazon MTurk platform (see Figure 1C),  
222 which enables efficient collection of large-scale psychophysical data from crowd-sourced  
223 “human intelligence tasks” (HITs). The reliability of the online MTurk platform has been  
224 validated by comparing results obtained from online and in-lab psychophysical experiments  
225 (Majaj et al., 2015; Rajalingham et al., 2015). We pooled 927,296 trials from 1472 human  
226 subjects to characterize the aggregate human behavior, which we refer to as the “pooled” human  
227 (or “archetypal” human). Each human subject performed only a small number of trials (~150) on  
228 a subset of the images and binary tasks. All 2400 images were used for behavioral testing, but in  
229 some of the HITs, we biased the image selection towards the 240 primary test images ( $1424 \pm 70$   
230 trials/image on this subsampled set, versus  $271 \pm 93$  trials/image on the remaining images, mean  $\pm$   
231 SD) to efficiently characterize behavior at image level resolution. Images were randomly drawn  
232 such that each human subject was exposed to each image a relatively small number of times  
233 ( $1.5 \pm 2.0$  trials/image per subject, mean  $\pm$  SD), in order to mitigate potential alternative  
234 behavioral strategies (e.g. “memorization” of images) that could arise from a finite image set.  
235 Behavioral signatures at the object-level (B.O1, B.O2, see *Behavioral metrics and signatures*)  
236 were measured using all 2400 test images, while image-level behavioral signatures (B.I1n, B.I2n,

237 see *Behavioral metrics and signatures*) were measured using the 240 primary test images. (We  
238 observed qualitatively similar results using those metrics on the full 2400 test images, but we  
239 here focus on the primary test images as the larger number of trials leads to lower noise levels).

240

241 Five other human subjects were separately recruited on MTurk to each perform a large  
242 number of trials on the same images and tasks ( $53,097 \pm 15,278$  trials/subject, mean  $\pm$  SD).  
243 Behavioral data from these five subjects was not included in the characterization of the pooled  
244 human described above, but instead aggregated together to characterize a distinct held-out  
245 human pool. For the scope of the current work, this held-out human pool—which largely  
246 replicated all behavioral signatures of the larger archetypal human (see Figures 2 and 3)—served  
247 as an independent validation of our human behavioral measurements.

248

#### 249 *Testing monkey behavior*

250 Five adult male rhesus macaque monkeys (*Macaca mulatta*, subjects *M*, *Z*, *N*, *P*, *B*) were  
251 tested on the same basic-level, core object recognition task paradigm described above, with  
252 minor modification as described below. All procedures were performed in compliance with  
253 National Institutes of Health guidelines and the standards of the Massachusetts Institute of  
254 Technology Committee on Animal Care and the American Physiological Society. To efficiently  
255 characterize monkey behavior, we used a novel home-cage behavioral system developed in our  
256 lab (termed MonkeyTurk, see Fig. 1C). This system leveraged a tablet touchscreen (9" Google  
257 Nexus or 10.5" Samsung Galaxy Tab S) and used a web application to wirelessly load the task  
258 and collect the data (code available at <https://github.com/dicarlolab/mkturk>). Analogous to the  
259 online Amazon Mechanical Turk, which allows for efficient psychophysical assays of a large  
260 number (hundreds) of human users in their native environments, MonkeyTurk allowed us to test  
261 many monkey subjects simultaneously in their home environment. Each monkey voluntarily  
262 initiated trials, and each readily performed the task a few hours each day that the task apparatus  
263 was made available to it. At an average rate of ~2,000 trials per day per monkey, we collected a  
264 total of 836,117 trials from the five monkey subjects over a period of ~3 months.

265

266 Monkey training is described in detail elsewhere (Rajalingham et al., 2015). Briefly, all  
267 monkeys were initially trained on the match-test-image-to-object rule using other images and

268 were also trained on discriminating the particular set of 24 objects tested here using a separate set  
269 of training images rendered from these objects, in the same manner as the main testing images.  
270 Two of the monkeys subjects (Z and M) were previously trained in the lab setting, and the  
271 remaining three subjects were trained using MonkeyTurk directly in their home cages and did  
272 not have significant prior lab exposure. Once monkeys reached saturation performance on  
273 training images, we began the behavioral testing phase to collect behavior on test images.  
274 Monkeys did improve throughout the testing phase, exhibiting an increase in performance  
275 between the first and second half of trials of  $4\% \pm 0.9\%$  (mean  $\pm$  SEM over five monkey subjects).  
276 However, the image-level behavioral signatures obtained from the first and the second halves of  
277 trials were highly correlated to each other (B.I1 noise-adjusted correlation of  $0.85 \pm 0.06$ , mean  $\pm$   
278 SEM over five monkey subjects, see *Behavioral metrics and signatures* below), suggesting that  
279 monkeys did not significantly alter strategies (e.g. did not “memorize” images) throughout the  
280 behavioral testing phase.

281

282 The monkey task paradigm was nearly identical to the human paradigm (see Figure 1B),  
283 with the exception that trials were initiated by touching a white “fixation” circle horizontally  
284 centered on the bottom third of the screen (to avoid occluding centrally-presented test images  
285 with the hand). This triggered a 100ms central presentation of a test image, followed  
286 immediately by the presentation of the two choice images (Fig. 1B, location of correct choice  
287 randomly assigned on each trial, identical to the human task). Unlike the main human task,  
288 monkeys responded by directly touching the screen at the location of one of the two choice  
289 images. Touching the choice image corresponding to the object shown in the test image resulted  
290 in the delivery of a drop of juice through a tube positioned at mouth height (but not obstructing  
291 view), while touching the distractor choice image resulted in a three second timeout. Because  
292 gaze direction typically follows the hand during reaching movements, we assumed that the  
293 monkeys were looking at the screen during touch interactions with the fixation or choice targets.  
294 In both the lab and in the home cage, we maintained total test image size at  $\sim 6$  degrees of visual  
295 angle at the center of gaze, and we took advantage of the retina-like display qualities of the tablet  
296 by presenting images pixel matched to the display (256 x 256 pixel image displayed using 256 x  
297 256 pixels on the tablet at a distance of 8 inches) to avoid filtering or aliasing effects.  
298

299 As with Mechanical Turk testing in humans, MonkeyTurk head-free home-cage testing  
300 enables efficient collection of reliable, large-scale psychophysical data but it likely does not yet  
301 achieve the level of experimental control that is possible in the head-fixed laboratory setting.  
302 However, we note that when subjects were engaged in home-cage testing, they reliably had their  
303 mouth on the juice tube and their arm positioned through an armhole. These spatial constraints  
304 led to a high level of head position trial-by-trial reproducibility during performance of the task  
305 paradigm. Furthermore, when subjects were in this position, they could not see other animals as  
306 the behavior box was opaque, and subjects performed the task at a rapid pace 40 trials/minute  
307 suggesting that they were not frequently distracted or interrupted. The location of the upcoming  
308 test image (but not the location of the object within that test image) was perfectly predictable at  
309 the start of each behavioral trial, which likely resulted in a reliable, reproduced gaze direction at  
310 the moment that each test image was presented. The relatively short—but natural and high  
311 performing (Cadieu et al., 2014)—test image duration (100 ms) ensured that saccadic eye  
312 movements were unlikely to influence test image performance (as they generally take ~200 ms to  
313 initiate in response to the test image, and thus well after the test image has been extinguished).

314

### 315 *Testing model behavior*

316 We tested a number of different deep convolutional neural network (DCNN) models on  
317 the exact same images and tasks as those presented to humans and monkeys. Importantly, our  
318 core object recognition task paradigm is closely analogous to the large-scale ImageNet 1000-way  
319 object categorization task for which these networks were optimized and thus expected to perform  
320 well. We focused on publicly available DCNN model architectures that have proven highly  
321 successful with respect to this computer vision benchmark over the past five years: AlexNet  
322 (Krizhevsky et al., 2012), NYU (Zeiler and Fergus, 2014), VGG (Simonyan and Zisserman,  
323 2014), GoogleNet (Szegedy et al., 2013), Resnet (He et al., 2016), and Inception-v3 (Szegedy et  
324 al., 2013). As this is only a subset of possible DCNN models, we refer to these as the DCNN<sub>IC</sub>  
325 (to denote ImageNet-Categorization) visual system model sub-family. For each of the publicly  
326 available model architectures, we first used ImageNet-categorization-trained model instances,  
327 either using publicly available trained model instances or training them to saturation on the 1000-  
328 way classification task in-house. Training took several days on 1-2 GPUs.

329

330        We then performed psychophysical experiments on each ImageNet-trained DCNN model  
331 to characterize their behavior on the exact same images and tasks as humans and monkeys. We  
332 first adapted these ImageNet-trained models to our 24-way object recognition task by re-training  
333 the final class probability layer (initially corresponding to the probability output of the 1000-way  
334 ImageNet classification task) while holding all other layers fixed. In practice, this was done by  
335 extracting features from the penultimate layer of each DCNN<sub>IC</sub> (i.e. top-most prior to class  
336 probability layer), on the same images that were presented to humans and monkeys, and training  
337 back-end multi-class logistic regression classifiers to determine the cross-validated output class  
338 probability for each image. This procedure is illustrated in Figure 1C. To estimate the hit rate of  
339 a given image in a given binary classification task, we renormalized the 24-way class  
340 probabilities of that image, considering only the two relevant classes, to sum to one. Object-level  
341 and image-level behavioral metrics were computed based on these hit rate estimates (as  
342 described in *Behavioral metrics and signatures* below). Importantly, this procedure assumes that  
343 the model “retina” layer processes the central 6 degrees of the visual field. It also assumes that  
344 linear discriminants (“readouts”) of the model’s top feature layer are its behavioral output (as  
345 intended by the model designers). Manipulating either of these choices (e.g. resizing the input  
346 images such that they span only part of the input layer, or building linear discriminates for  
347 behavior using a different model feature layer) would result in completely new, testable ANN  
348 models that we do not test here.

349

350        From these analyses, we selected the most *human-consistent* DCNN<sub>IC</sub> architecture  
351 (Inception-v3, see *Behavioral consistency* below), fixed that architecture, and then performed  
352 post-hoc analyses in which we varied: the input image sampling, the initial parameter settings  
353 prior to training, the filter training images, the type of classifiers used to generate the behavior  
354 from the model features, and the classifier training images. To examine input image sampling,  
355 we re-trained the Inception-v3 architecture on images from ImageNet that were first spatially  
356 filtered to match the spatial sampling of the primate retina (i.e. an approximately exponential  
357 decrease in cone density away from the fovea) by effectively simulating a fish-eye  
358 transformation on each image. These images were at highest resolution at the “fovea” (i.e. center  
359 of the image) with gradual decrease in resolution with increasing eccentricity. To examine the  
360 analog of “inter-subject variability”, we constructed multiple trained model instances

361 (“subjects”), where the architecture and training images were held fixed (Inception-v3 and  
362 ImageNet, respectively) but the model filter weights initial condition and order of training  
363 images were randomly varied for each model instance. Importantly, this procedure is only one  
364 possible choice for simulating inter-subject variability for DCNN models, a choice that is an  
365 important open research direction that we do not address here. To examine the effect of model  
366 training, we fine-tuned an ImageNet-trained Inception-v3 model on a synthetic image set  
367 consisting of ~6.9 million images of 1049 objects (holding out 50,000 images for model  
368 validation). These images were generated using the same rendering pipeline as our test images,  
369 but the objects were non-overlapping with the 24 test objects presented here. As expected, fine-  
370 tuning on synthetic images led to an overall increase in performance of ~5%. We tested the effect  
371 of different classifiers to generate model behavior by testing both multi-class logistic regression  
372 and support vector machine classifiers. Additionally, we tested the effect of varying the number  
373 of training images used to train those classifiers (20 versus 50 images per class).

374

### 375 *Behavioral metrics and signatures*

376 To characterize the behavior of any visual system, we here introduce four behavioral ( $B$ )  
377 metrics of increasing richness, requiring increasing amounts of data to measure reliably. Each  
378 behavioral metric computes a pattern of unbiased behavioral performance, using a sensitivity  
379 index:  $d' = Z(\text{HitRate}) - Z(\text{FalseAlarmRate})$ , where  $Z$  is the inverse of the cumulative  
380 Gaussian distribution. The various metrics differ in the resolution at which hit rates and false  
381 alarm rates are computed. Table 1 summarizes the four behavioral metrics, varying the hit-rate  
382 resolution (object-level or image-level) and the false-alarm resolution (one-versus-all or one-  
383 versus-other). When each metric is applied to the behavioral data of a visual system—biological  
384 or artificial—we refer to the result as one behavioral “signature” of that system. Note that we do  
385 not consider the signatures obtained here to be the final say on the behavior of these biological or  
386 artificial systems—in the terms defined here, new experiments using new objects/images but the  
387 same metrics would produce additional behavioral signatures.

388

389 The four behavioral metrics we chose are as follows: First, the one-versus-all object-level  
390 performance metric (termed B.O1) estimates the discriminability of each object from all other  
391 objects, pooling across all distractor object choices. Since we here tested 24 objects, the resulting

392 B.O1 signature has 24 independent values. Second, the one-versus-other object-level  
393 performance metric (termed B.O2) estimates the discriminability of each specific pair of objects,  
394 or the pattern of pairwise object confusions. Since we here tested 276 interleaved binary object  
395 discrimination tasks, the resulting B.O2 signature has 276 independent values (the off-diagonal  
396 elements on one half of the 24x24 symmetric matrix). Third, the one-versus-all image-level  
397 performance metric (termed B.I1) estimates the discriminability of each image from all other  
398 objects, pooling across all possible distractor choices. Since we here focused on the primary  
399 image test set of 240 images (10 per object, see above), the resulting B.I1 signature has 240  
400 independent values. Fourth, the one-versus-other image-level performance metric (termed B.I2)  
401 estimates the discriminability of each image from each distractor object. Since we here focused  
402 on the primary image test set of 240 images (10 per object, see above) with 23 distractors, the  
403 resulting B.I2 signature has 5520 independent values.

404

405 Naturally, object-level and image-level behavioral signatures are tightly linked. For  
406 example, images of a particularly difficult-to-discriminate object would inherit lower  
407 performance values on average as compared to images from a less difficult-to-discriminate  
408 object. To isolate the behavioral variance that is specifically driven by image variation and not  
409 simply predicted by the objects (and thus already captured by B.O1 and B.O2), we defined  
410 normalized image-level behavioral metrics (termed B.I1n, B.I2n) by subtracting the mean  
411 performance values over all images of the same object and task. This process is schematically  
412 illustrated in Figure 3A. We note that the resulting normalized image-level behavioral signatures  
413 capture a significant proportion of the total image-level behavioral variance in our data (e.g.  
414 52%, 58% of human B.I1 and B.I2 variance is driven by image variation, independent of object  
415 identity). In this study, we use these normalized metrics for image-level behavioral comparisons  
416 between models and primates (see Results).

417

#### 418 *Behavioral Consistency*

419 To quantify the similarity between a model visual system and the human visual system  
420 with respect to a given behavioral metric, we used a measure called the “*human-consistency*” as  
421 previously defined (Johnson et al., 2002). *Human-consistency* ( $\tilde{\rho}$ ) is computed, for each of the  
422 four behavioral metrics, as a noise-adjusted correlation of behavioral signatures (DiCarlo and

423 Johnson, 1999). For each visual system, we randomly split all behavioral trials into two equal  
424 halves and applied each behavioral metric to each half, resulting in two independent estimates of  
425 the system's behavioral signature with respect to that metric. We took the Pearson correlation  
426 between these two estimates of the behavioral signature as a measure of the reliability of that  
427 behavioral signature given the amount of data collected, i.e. the split-half internal reliability. To  
428 estimate the *human-consistency*, we computed the Pearson correlation over all the independent  
429 estimates of the behavioral signature from the model (**m**) and the human (**h**), and we then divide  
430 that raw Pearson correlation by the geometric mean of the split-half internal reliability of the  
431 same behavioral signature measured for each system:  $\tilde{\rho}(\mathbf{m}, \mathbf{h}) = \frac{\rho(\mathbf{m}, \mathbf{h})}{\sqrt{\rho(\mathbf{m}, \mathbf{m})\rho(\mathbf{h}, \mathbf{h})}}$ .

432

433 Since all correlations in the numerator and denominator were computed using the same  
434 amount of trial data (exactly half of the trial data), we did not need to make use of any prediction  
435 formulas (e.g. extrapolation to larger number of trials using Spearman-Brown prediction  
436 formula). This procedure was repeated 10 times with different random split-halves of trials. Our  
437 rationale for using a reliability-adjusted correlation measure for *human-consistency* was to  
438 account for variance in the behavioral signatures that arises from “noise,” i.e., variability that is  
439 not replicable by the experimental condition (image and task) and thus that no model can be  
440 expected to predict (DiCarlo and Johnson, 1999; Johnson et al., 2002). In sum, if the model (m)  
441 is a replica of the archetypal human (h), then its expected human-consistency is 1.0, regardless of  
442 the finite amount of data that are collected.

443

#### 444 *Characterization of Residuals*

445 In addition to measuring the similarity between the behavioral signatures of primates and  
446 models (using *human-consistency* analyses, as described above), we examined the corresponding  
447 differences, termed “residual signatures.” Each candidate visual system model’s residual  
448 signature was estimated as the residual of a linear least squares regression of the model’s  
449 signature on the corresponding human signature and a free intercept parameter. This procedure  
450 effectively captures the differences between human and model signatures after accounting for  
451 overall performance differences. Residual signatures were estimated on disjoint split-halves of  
452 trials, repeating 10 times with random trial permutations. Residuals were computed with respect  
453 to the normalized one-versus-all image-level performance metric (B.I1n) as this metric showed a

454 clear difference between DCNN<sub>IC</sub> models and primates, and the behavioral residual can be  
455 interpreted based only the test images (i.e. we can assign a residual per image).

456  
457 To examine the extent to which the difference between each model and the archetypal  
458 human is reliably shared across different models, we measured the Pearson correlation between  
459 the residual signatures of pairs of models. Residual similarity was quantified as the proportion of  
460 shared variance, defined as the square of the noise-adjusted correlation between residual  
461 signatures (the noise-adjustment was done as defined in equation above). Correlations of residual  
462 signatures were always computed across distinct split-halves of data, to avoid introducing  
463 spurious correlations from subtracting common noise in the human data. We measured the  
464 residual similarity between all pairs of tested models, holding both architecture and optimization  
465 procedure fixed (between instances of the ImageNet-categorization trained Inception-v3 model,  
466 varying in filter initial conditions), varying the architecture while holding the optimization  
467 procedure fixed (between all tested ImageNet-categorization trained DCNN architectures), and  
468 holding the architecture fixed while varying the optimization procedure (between ImageNet-  
469 categorization trained Inception-v3 and synthetic-categorization fine-tuned Inception-v3  
470 models). This analysis addresses not only the reliability of the failure of DCNN<sub>IC</sub> models to  
471 predict human behavior (deviations from humans), but also the relative importance of the  
472 characteristics defining similarities within the model sub-family (namely, the architecture and the  
473 optimization procedure). We first performed this analysis for residual signatures over the 240  
474 primary test images, and subsequently zoomed in on subsets of images that humans found to be  
475 particularly difficult. This image selection was made relative to the distribution of image-level  
476 performance of held-out human subjects (B.I1 metric from five subjects); difficult images were  
477 defined as ones with performance below the 25<sup>th</sup> percentile of this distribution.

478  
479 To examine whether the difference between each model and humans can be explained by  
480 simple human-interpretable stimulus attributes, we regressed each DCNN<sub>IC</sub> model's residual  
481 signature on image attributes (object size, eccentricity, pose, and contrast). Briefly, we  
482 constructed a design matrix from the image attributes (using individual attributes, or all  
483 attributes), and used multiple linear least squares regression to predict the image-level residual  
484 signature. The multiple linear regression was tested using two-fold cross-validation over trials.

485 The relative importance of each attribute (or groups of attributes) was quantified using the  
486 proportion of explainable variance (i.e. variance remaining after accounting for noise variance)  
487 explained from the residual signature.

488

#### 489 *Primate behavior zone*

490 In this work, we are primarily concerned with the behavior of an “archetypal human”,  
491 rather than the behavior of any given individual human subject. We operationally defined this  
492 concept as the common behavior over many humans, obtained by pooling together trials from a  
493 large number of individual human subjects and treating this human pool as if it were acquired  
494 from a single behaving agent. Due to inter-subject variability, we do not expect any given human  
495 or monkey subject to be perfectly consistent with this archetypal human (i.e. we do not expect it  
496 to have a *human-consistency* of 1.0). Given current limitations of monkey psychophysics, we are  
497 not yet able to measure the behavior of very large number of monkey subjects at high resolution  
498 and consequently cannot directly estimate the *human-consistency* of the corresponding  
499 “archetypal monkey” to the human pool. Rather, we indirectly estimated this value by first  
500 measuring *human-consistency* as a function of number of individual monkey subjects pooled  
501 together (n), and extrapolating the *human-consistency* estimate for pools of very large number of  
502 subjects (as n approaches infinity). Extrapolations were done using least squares fitting of an  
503 exponential function  $\tilde{\rho}(n) = a + b \cdot e^{-cn}$  (see Figure 4).

504

505 For each behavioral metric, we defined a “primate zone” as the range of *human-*  
506 *consistency* values delimited by estimates  $\tilde{\rho}_{M\infty}$  and  $\tilde{\rho}_{H\infty}$  as lower and upper bounds respectively.  
507  $\tilde{\rho}_{M\infty}$  corresponds to the extrapolated estimate of *human-consistency* of a large (i.e. infinitely  
508 many) pool of rhesus macaque monkeys;  $\tilde{\rho}_{H\infty}$  is by definition equal to 1.0. Thus, the primate  
509 zone defines a range of *human-consistency* values that correspond to models that accurately  
510 capture the behavior of the human pool, at least as well as an extrapolation of our monkey  
511 sample. In this work, we defined this range of *human-consistency* values as the criterion for  
512 success for computational models of primate visual object recognition behavior.

513

514 To make a global statistical inference about whether models sampled from the DCNN<sub>IC</sub>  
515 sub-family meet or fall short of this criterion for success, we attempted to reject the hypothesis

516 that, for a given behavioral metric, the *human-consistency* of DCNN<sub>IC</sub> models is within the  
517 primate zone. To test this hypothesis, we estimated the empirical probability that the distribution  
518 of *human-consistency* values, estimated over different model instances within this family, could  
519 produce *human-consistency* values within the primate zone. Specifically, we estimated a p-value  
520 for each behavioral metric using the following procedure: We first estimated an empirical  
521 distribution of Fisher-transformed *human-consistency* values for this model family (i.e. over all  
522 tested DCNN<sub>IC</sub> models and over all trial-resampling of each DCNN<sub>IC</sub> model). From this  
523 empirical distribution, we fit a Gaussian kernel density function, optimizing the bandwidth  
524 parameter to minimize the mean squared error to the empirical distribution. This kernel density  
525 function was evaluated to compute a p-value, by computing the cumulative probability of  
526 observing a *human-consistency* value greater than or equal to the criterion of success (i.e. the  
527 Fisher transformed  $\tilde{\rho}_{M\infty}$  value). This p-value indicates the probability that *human-consistency*  
528 values sampled from the observed distribution would fall into the primate zone, with smaller p-  
529 values indicating stronger evidence against the hypothesis that the *human-consistency* of DCNN  
530 models is within the primate zone.

531

## 532 RESULTS

533

534 In the present work, we systematically compared the basic level core object recognition  
535 behavior of primates and state-of-the-art artificial neural network models using a series of  
536 behavioral metrics ranging from low to high resolution within a two-alternative forced choice  
537 match-to-sample paradigm. The behavior of each visual system, whether biological or artificial,  
538 was tested on the same 2400 images (24 objects, 100 images/object) in the same 276 interleaved  
539 binary object recognition tasks. Each system's behavior was characterized at multiple resolutions  
540 (see *Behavioral metrics and signatures* in Methods) and directly compared to the corresponding  
541 behavioral metric applied on the archetypal human (defined as the average behavior of a large  
542 pool of human subjects tested; see Methods). The overarching logic of this study was that, if two  
543 visual systems are equivalent, they should produce statistically indistinguishable behavioral  
544 signatures with respect to these metrics. Specifically, our goal was to compare the behavioral  
545 signatures of visual system models with the corresponding behavioral signatures of primates.

546

547 *Object-level behavioral comparison*

548 We first examined the pattern of one-versus-all object-level behavior (termed “B.O1  
549 metric”) computed across all images and possible distractors. Since we tested 24 objects here, the  
550 B.O1 signature was 24 dimensional. Figure 2A shows the B.O1 signatures for the pooled human  
551 (pooling n=1472 human subjects), pooled monkey (pooling n=5 monkey subjects), and several  
552 DCNN<sub>IC</sub> models as 24-dimensional vectors using a color scale. Each element of the vector  
553 corresponds to the system’s discriminability of one object against all others that were tested (i.e.  
554 all other 23 objects). The color scales span each signature’s full performance range, and warm  
555 colors indicate lower discriminability. For example, red indicates that the tested visual system  
556 found the object corresponding to that element of the vector to be very challenging to  
557 discriminate from other objects (on average over all 23 discrimination tests, and on average over  
558 all images). Figure 2B directly compares the B.O1 signatures computed from the behavioral  
559 output of two visual system models—a pixel model (top panel) and a DCNN<sub>IC</sub> model (Inception-  
560 v3, bottom panel)—against that of the human B.O1 signature. We observe a tighter  
561 correspondence to the human behavioral signature for the DCNN<sub>IC</sub> model visual system than for  
562 the baseline pixel model visual system. We quantified that similarity using a noise-adjusted  
563 correlation between each pair of B.O1 signatures (termed *human-consistency*, following  
564 (Johnson et al., 2002)); the noise adjustment means that a visual system that is identical to the  
565 human pool will have an expected *human-consistency* score of 1.0, even if it has irreducible trial-  
566 by-trial stochasticity; see Methods). Figure 2C shows the B.O1 *human-consistency* for each of  
567 the tested model visual systems. We additionally tested the behavior of a held-out pool of five  
568 human subjects (black dot) and a pool of five macaque monkey subjects (gray dot), and we  
569 observed that both yielded B.O1 signatures that were highly human-consistent (*human-  
570 consistency*  $\tilde{\rho} = 0.90, 0.97$  for monkey pool and held-out human pool, respectively). We defined  
571 a range of *human-consistency* values, termed the “primate zone” (shaded gray area), delimited by  
572 extrapolated *human-consistency* estimates of large pools of macaques (see Methods, Figure 4).  
573 We found that the baseline pixel visual system model and the low-level V1 visual system model  
574 were not within this zone ( $\tilde{\rho} = 0.40, 0.67$  for pixels and V1 models, respectively), while all tested  
575 DCNN<sub>IC</sub> visual system models were either within or very close to this zone. Indeed, we could not  
576 reject the hypothesis that DCNN<sub>IC</sub> models are primate-like ( $p = 0.54$ , exact test, see Methods).  
577

578 Next, we compared the behavior of the visual systems at a slightly higher level of  
579 resolution. Specifically, instead of pooling over all discrimination tasks for each object, we  
580 computed the mean discriminability of each of the 276 pairwise discrimination tasks (still  
581 pooling over images within each of those tasks). This yielded a symmetric matrix that is referred  
582 to here as the B.O2 signature. Figure 2D shows the B.O2 signatures of the pooled human, pooled  
583 monkey, and several DCNN<sub>IC</sub> visual system models as 24x24 symmetric matrices. Each bin ( $i, j$ )  
584 corresponds to the system's discriminability of objects  $i$  and  $j$ , where warmer colors indicate  
585 lower performance; color scales are not shown but span each signature's full range. We observed  
586 strong qualitative similarities between the pairwise object confusion patterns of all of the high  
587 level visual systems (e.g. camel and dog are often confused with each other by all three systems).  
588 This similarity is quantified in Figure 2E, which shows the *human-consistency* of all examined  
589 visual system models with respect to this metric. Similar to the B.O1 metric, we observed that  
590 both a pool of macaque monkeys and a held-out pool of humans are highly *human-consistent*  
591 with respect to this metric ( $\tilde{\rho} = 0.77, 0.94$  for monkeys, humans respectively). Also similar to the  
592 B.O1 metric, we found that all DCNN<sub>IC</sub> visual system models are highly *human-consistent* ( $\tilde{\rho} >$   
593 0.8) while the baseline pixel visual system model and the low-level V1 visual system model were  
594 not ( $\tilde{\rho} = 0.41, 0.57$  for pixels, V1 models respectively). Indeed, all DCNN<sub>IC</sub> visual system  
595 models are within the defined “primate zone” of *human-consistency*, and we could not falsify the  
596 hypothesis that DCNN<sub>IC</sub> models are primate-like ( $p = 0.99$ , exact test).

597

598 Taken together, humans, monkeys, and current DCNN<sub>IC</sub> models all share similar patterns  
599 of object-level behavioral performances (B.O1 and B.O2 signatures) that are not shared with  
600 lower-level visual representations (pixels and V1). However, object-level performance patterns  
601 do not capture the fact that some images of an object are more challenging than other images of  
602 the same object because of interactions of the variation in the object's pose and position with the  
603 object's class. To overcome this limitation, we next examined the patterns of behavior at the  
604 resolution of individual images on a subsampled set of images where we specifically obtained a  
605 large number of behavioral trials to accurately estimate behavioral performance on each image.  
606 Note that, from the point of view of the subjects, the behavioral tasks are identical to those  
607 already described. We simply aimed to measure and compare their patterns of performance at  
608 much higher resolution.

609

610 *Image-level behavioral comparison*

611 To isolate purely image-level behavioral variance, i.e. variance that is not predicted by  
612 the object and thus already captured by the B.O1 signature, we computed the normalized image-  
613 level signature. This normalization procedure is schematically illustrated in Figure 3A which  
614 shows that the one-versus-all image-level signature (240-dimensional, 10 images/object) is used  
615 to obtain the normalized one-versus-all image-level signature (termed B.I1n, see *Behavioral*  
616 *metrics and signatures*). Figure 3B shows the B.I1n signatures for the pooled human, pooled  
617 monkey, and several DCNN<sub>IC</sub> models as 240 dimensional vectors. Each bin's color corresponds  
618 to the discriminability of a single image against all distractor options (after subtraction of object-  
619 level discriminability, see Figure 3A), where warmer colors indicate lower values; color scales  
620 are not shown but span each signature's full range. Figure 3D shows the *human-consistency* with  
621 respect to the B.I1n signature for all tested models. Unlike with object-level behavioral metrics,  
622 we now observe a divergence between DCNN<sub>IC</sub> models and primates. Both the monkey pool and  
623 the held-out human pool remain highly *human-consistent* ( $\tilde{\rho} = 0.77, 0.96$  for monkeys, humans  
624 respectively), but all DCNN<sub>IC</sub> models were significantly less *human-consistent* (Inception-  
625 v3:  $\tilde{\rho} = 0.62$ ) and well outside of the defined “primate zone” of B.I1n *human-consistency*.  
626 Indeed, the hypothesis that the *human-consistency* of DCNN<sub>IC</sub> models is within the primate zone  
627 is strongly rejected ( $p = 6.16e-8$ , exact test, see Methods).

628

629 We can zoom in further by examining not only the overall performance for a given image  
630 but also the object confusions for each image, i.e. the additional behavioral variation that is due  
631 not only to the test image but to the interaction of that test image with the alternative (incorrect)  
632 object choice that is provided after the test image (see Fig. 1B). This is the highest level of  
633 behavioral accuracy resolution that our task design allows. In raw form, it corresponds to one-  
634 versus-other image-level confusion matrix, where the size of that matrix is the total number of  
635 images by the total number of objects (here, 240x24). Each bin  $(i,j)$  corresponds to the behavioral  
636 discriminability of a single image  $i$  against distractor object  $j$ . Again, we isolate variance that is  
637 not predicted by object-level performance by subtracting the average performance on this binary  
638 task (mean over all images) to convert the raw matrix B.I2 above into the normalized matrix,  
639 referred to as B.I2n. Figure 3D shows the B.I2n signatures as 240x24 matrices for the pooled

640 human, pooled monkey and top DCNN<sub>IC</sub> visual system models. Color scales are not shown but  
641 span each signature's full range; warmer colors correspond to images with lower performance in  
642 a given binary task, relative to all images of that object in the same task. Figure 3E shows the  
643 *human-consistency* with respect to the B.I2n metric for all tested visual system models.  
644 Extending our observations using B.I1n, we observe a similar divergence between primates and  
645 DCNN<sub>IC</sub> visual system models on the matrix pattern of image-by-distractor difficulties (B.I2n).  
646 Specifically, both the monkey pool and held-out human pool remain highly *human-consistent*  
647 ( $\tilde{\rho} = 0.75, 0.77$  for monkeys, humans respectively), while all tested DCNN<sub>IC</sub> models are  
648 significantly less *human-consistent* (Inception-v3:  $\tilde{\rho} = 0.53$ ) falling well outside of the defined  
649 “primate zone” of B.I2n *human-consistency* values. Once again, the hypothesis that the *human-*  
650 *consistency* of DCNN<sub>IC</sub> models is within the primate zone is strongly rejected ( $p = 3.17e-18$ ,  
651 exact test, see Methods).

652

### 653 *Natural subject-to-subject variation*

654 For each behavioral metric (B.O1, BO2, B.I1n, BI2n), we defined a “primate zone” as the  
655 range of consistency values delimited by *human-consistency* estimates  $\tilde{\rho}_{M\infty}$  and  $\tilde{\rho}_{H\infty}$  as lower  
656 and upper bounds respectively.  $\tilde{\rho}_{M\infty}$  corresponds to the extrapolated estimate of the *human-*  
657 *consistency* of a large (i.e. infinitely many subjects) pool of rhesus macaque monkeys. Thus, the  
658 fact that a particular tested visual system model falls outside of the primate zone can be  
659 interpreted as a failure of that visual system model to accurately predict the behavior of the  
660 archetypal human at least as well as the archetypal monkey.

661

662 However, from the above analyses, it is not yet clear whether a visual system model that  
663 fails to predict the archetypal human might nonetheless accurately correspond to one or more  
664 individual human subjects found within the natural variation of the human population. Given the  
665 difficulty of measuring individual subject behavior at the resolution of single images for large  
666 numbers of human and monkey subjects, we could not yet directly test this hypothesis. Instead,  
667 we examined it indirectly by asking whether an archetypal model—that is a pool that includes an  
668 increasing number of model “subjects”—would approach the human pool. We simulated model  
669 inter-subject variability by retraining a fixed DCNN architecture with a fixed training image set  
670 with random variation in the initial conditions and order of training images. This procedure

671 results in models that can still perform the task but with slightly different learned weight values.  
672 We note that this procedure is only one possible choice of generating inter-subject variability  
673 within each visual system model type, a choice that is an important open research direction that  
674 we do not address here. From this procedure, we constructed multiple trained model instances  
675 (“subjects”) for a fixed DCNN architecture, and asked whether an increasingly large pool of  
676 model “subjects” better captures the behavior of the human pool, at least as well as a monkey  
677 pool. This post-hoc analysis was conducted for the most *human-consistent* DCNN architecture  
678 (Inception-v3).

679

680 Figure 4A shows, for each of the four behavioral metrics, the measured *human-*  
681 *consistency* of subject pools of varying size (number of subjects  $n$ ) of rhesus macaque monkeys  
682 (black) and ImageNet-trained Inception-v3 models (blue). The *human-consistency* increases with  
683 growing number of subjects for both visual systems across all behavioral metrics. To estimate  
684 the expected *human-consistency* for a pool of infinitely many monkey or model subjects, we fit  
685 an exponential function mapping  $n$  to the mean *human-consistency* values and obtained a  
686 parameter estimate for the asymptotic value (see Methods). We note that estimated asymptotic  
687 values are not significantly beyond the range of the measured data—the *human-consistency* of a  
688 pool of five monkey subjects reaches within 97% of the *human-consistency* of an estimated  
689 infinite pool of monkeys for all metrics—giving credence to the extrapolated *human-consistency*  
690 values. This analysis suggests that under this model of inter-subject variability, a pool of  
691 Inception-v3 subjects accurately capture archetypal human behavior at the resolution of objects  
692 (B.O1, B.O2) by our primate zone criterion (see Figure 4A, first two panels). In contrast, even a  
693 large pool of Inception-v3 subjects still fails at its final asymptote to accurately capture human  
694 behavior at the image-level (B.I1n, B.I2n) (Figure 4A, last two panels).

695

#### 696 *Modification of visual system models to try to rescue their human-consistency*

697 Next, we wondered if some relatively simple changes to the DCNN<sub>IC</sub> visual system  
698 models tested here could bring them into better correspondence with the primate visual system  
699 behavior (with respect to B.I1n and B.I2n metrics). Specifically, we considered and tested the  
700 following modifications to the most *human-consistent* DCNN<sub>IC</sub> model visual system (Inception-  
701 v3): we (1) changed the input to the model to be more primate-like in its retinal sampling

702 (Inception-v3 + retina-like), (2) changed the transformation (aka “decoder”) from the internal  
703 model feature representation into the behavioral output by augmenting the number of decoder  
704 training images or changing the decoder type (Inception-v3 + SVM, Inception-v3 +  
705 classifier\_train), and (3) modified all of the internal filter weights of the model (aka “fine  
706 tuning”) by augmenting its ImageNet training with additional images drawn from the same  
707 distribution as our test images (Inception-v3 + synthetic-fine-tune). While some of these  
708 modifications (e.g. fine-tuning on synthetic images and increasing the number of classifier  
709 training images) had the expected effect of increasing mean overall performance (not shown, see  
710 Methods), we found that none of these modifications led to a significant improvement in its  
711 *human-consistency* on the behavioral metrics (Figure 4B). Thus, the failure of current DCNN<sub>IC</sub>  
712 models to accurately capture the image-level signatures of primates cannot be rescued by simple  
713 modifications on a fixed architecture.

714

#### 715 *Looking for clues: Image-level comparisons of models and primates*

716 Taken together, Figures 2, 3 and 4 suggest that current DCNN<sub>IC</sub> visual system models fail  
717 to accurately capture the image-level signatures of humans and monkeys. To further examine this  
718 failure in the hopes of providing clues for model improvement, we examined the image-level  
719 residual signatures of all the visual system models, relative to the pooled human. For each model,  
720 we computed its residual signature as the difference (positive or negative) of a linear least  
721 squares regression of the model signature on the corresponding human signature. For this  
722 analysis, we focused on the B.I1n metric as it showed a clear divergence of DCNN<sub>IC</sub> models and  
723 primates, and the behavioral residual can be interpreted based only on the test images (whereas  
724 B.I2n depends on the interaction between test images and distractor choice).

725

726 We first asked to what extent the residual signatures are shared between different visual  
727 system models. Figure 5A shows the similarity between the residual signatures of all pairs of  
728 models; the color of bin  $(i,j)$  indicates the proportion of explainable variance that is shared  
729 between the residual signatures of visual systems  $i$  and  $j$ . For ease of interpretation, we ordered  
730 visual system models based on their architecture and optimization procedure and partitioned this  
731 matrix into four distinct regions. Each region compares the residuals of a “source” model group  
732 with fixed architecture and optimization procedure (five Inception-v3 models optimized for

733 categorization on ImageNet, varying only in initial conditions and training image order) to a  
734 “target” model group. The target groups of models for each of the four regions are: 1) the pooled  
735 monkey, 2) other DCNN<sub>IC</sub> models from the source group, 3) DCNN<sub>IC</sub> models that differ in  
736 architecture but share the optimization procedure of the source group models and 4) DCNN<sub>IC</sub>  
737 models that differ slightly using an augmented optimization procedure but share the architecture  
738 of the source group models. Figure 5B shows the mean ( $\pm$ SD) variance shared in the residuals  
739 averaged within these four regions for all images (black dots), as well as for images that humans  
740 found to be particularly difficult (gray dots, selected based on held-out human data, see  
741 Methods). First, consistent with the results shown in Figure 3, we note that the residual  
742 signatures of this particular DCNN<sub>IC</sub> model are not well shared with the pooled monkey ( $r^2=0.39$   
743 in region 1), and this phenomenon is more pronounced for the images that humans found most  
744 difficult ( $r^2=0.17$  in region 1). However, this relatively low correlation between model and  
745 primate residuals is not indicative of spurious model residuals, as the model residual signatures  
746 were highly reliable between different instances of this fixed DCNN<sub>IC</sub> model, across random  
747 training initializations (region 2:  $r^2=0.79$ , 0.77 for all and most difficult images, respectively).  
748 Interestingly, residual signatures were still largely shared with other DCNN<sub>IC</sub> models with vastly  
749 different architectures (region 3:  $r^2=0.70$ , 0.65 for all and most difficult images, respectively).  
750 However, residual signatures were more strongly altered when the visual training diet of the  
751 same architecture was altered (region 4:  $r^2=0.57$ , 0.46 for all and most difficult images  
752 respectively, cf. region 3). Taken together, these results indicate that the images where DCNN<sub>IC</sub>  
753 visual system models diverged from humans (and monkeys) were not spurious but were rather  
754 highly reliable across different model architectures, demonstrating that current DCNN<sub>IC</sub> models  
755 systematically and similarly diverge from primates.

756

757 To look for clues for model improvement, we asked what, if any, characteristics of  
758 images might account for this divergence of models and primates. We regressed the residual  
759 signatures of DCNN<sub>IC</sub> models on four different image attributes (corresponding to the size,  
760 eccentricity, pose, and contrast of the object in each image). We used multiple linear regressions  
761 to predict the model residual signatures from all of these image attributes, and also considered  
762 each attribute individually using simple linear regressions. Figure 6A shows example images  
763 (sampled from the full set of 2400 images) with increasing attribute value for each of these four

764 image attributes. While the DCNN<sub>IC</sub> models were not directly optimized to display primate-like  
765 performance dependence on such attributes, we observed that the Inception-v3 visual system  
766 model nonetheless exhibited qualitatively similar performance dependencies as primates (see  
767 Figure 6B). For example, humans (black), monkeys (gray) and the Inception-v3 model (blue) all  
768 performed better, on average, for images in which the object is in the center of gaze (low  
769 eccentricity) and large in size. Furthermore, all three systems performed better, on average, for  
770 images when the pose of the object was closer to the canonical pose (see Figure 6B); this  
771 sensitivity to object pose manifested itself as a non-linear dependence due to the fact that all  
772 tested objects exhibited symmetry in at least one axis. The similarity of the patterns in Figure 6B  
773 between primates and the DCNN<sub>IC</sub> visual system models is not perfect but is striking,  
774 particularly in light of the fact that these models were not optimized to produce these patterns.  
775 However, this similarity is analogous to the similarity in the B.O1 and B.O2 metrics in that it  
776 only holds on average over many images. Looking more closely at the image-by-image  
777 comparison, we again found that the DCNN<sub>IC</sub> models failed to capture a large portion of the  
778 image-by-image variation (Figure 3). In particular, Figure 6C shows the proportion of variance  
779 explained by specific image attributes for the residual signatures of monkeys (black) and  
780 DCNN<sub>IC</sub> models (blue). We found that, taken together, all four of these image attributes  
781 explained only ~10% of the variance in DCNN<sub>IC</sub> residual signatures, and each individual  
782 attribute could explain at most a small amount of residual variance (<5% of the explainable  
783 variance). In sum, these analyses show that some behavioral effects that might provide intuitive  
784 clues to modify the DCNN<sub>IC</sub> models are already in place in those models (e.g. a dependence on  
785 eccentricity). But the quantitative image-by-image analyses of the remaining unexplained  
786 variance (Figure 6C) argue that the DCNN<sub>IC</sub> visual system models' failure to capture primate  
787 image-level signatures cannot be further accounted for by these simple image attributes and  
788 likely stem from other factors.

789

## 790 **DISCUSSION**

791

792 The current work was motivated by the broad scientific goal of discovering models that  
793 quantitatively explain the neuronal mechanisms underlying primate invariant object recognition  
794 behavior. To this end, previous work had shown that specific artificial neural network models

795 (ANNs), drawn from a large family of deep convolutional neural networks (DCNNs) and  
796 optimized to achieve high levels of object categorization performance on large-scale image-sets,  
797 capture a large fraction of the variance in primate visual recognition behaviors (Rajalingham et  
798 al., 2015; Jozwik et al., 2016; Kheradpisheh et al., 2016; Kubilius et al., 2016; Peterson et al.,  
799 2016; Wallis et al., 2017), and the internal hidden neurons of those same models also predict a  
800 large fraction of the image-driven response variance of brain activity at multiple stages of the  
801 primate ventral visual stream (Yamins et al., 2013; Cadieu et al., 2014; Khaligh-Razavi and  
802 Kriegeskorte, 2014; Yamins et al., 2014; Güçlü and van Gerven, 2015; Cichy et al., 2016; Hong  
803 et al., 2016; Seibert et al., 2016; Cadena et al., 2017; Wen et al., 2017). For clarity, we here  
804 referred to this sub-family of models as DCNN<sub>IC</sub> (to denote ImageNet-Categorization training),  
805 so as to distinguish them from all possible models in the DCNN family, and more broadly, from  
806 the super-family of all ANNs. In this work, we directly compared leading DCNN<sub>IC</sub> models to  
807 primates (humans and monkeys) with respect to their behavioral signatures at both object and  
808 image level resolution in the domain of core object recognition. In order to do so, we measured  
809 and characterized primate behavior at larger scale and higher resolution than previously possible.  
810 We first replicate prior work (Rajalingham et al., 2015) showing that, at the object level,  
811 DCNN<sub>IC</sub> models produce statistically indistinguishable behavior from primates, and we extend  
812 that work by showing that these models also match the *average* primate sensitivities to object  
813 contrast, eccentricity, size, and pose, a noteworthy similarity in light of the fact that these models  
814 were not optimized to produce these performance patterns. However, our primary novel result is  
815 that, examining behavior at the higher resolution of individual images, all leading DCNN<sub>IC</sub>  
816 models failed to replicate the image-level behavioral signatures of primates. An important related  
817 claim is that rhesus monkeys are more consistent with the archetypal human than any of the  
818 tested DCNN<sub>IC</sub> models (at the image-level).

819  
820 While it had previously been shown that DCNN<sub>IC</sub> models can diverge from human  
821 behavior on specifically chosen adversarial images (Szegedy et al., 2013), a strength of our work  
822 is that we did not optimize images to induce failure but instead randomly sampled the image  
823 generative parameter space broadly. As such, our results highlight a *general*, rather than  
824 adversarial-induced, failure of DCNN<sub>IC</sub> models to fully capture the neural mechanisms  
825 underlying primate core object recognition behavior. Furthermore, we showed that this failure of

826 current DCNN<sub>IC</sub> models cannot be explained by simple image attributes and cannot be rescued  
827 by simple model modifications (input image sampling, model training, and classifier variations).  
828 Taken together, these results suggest that new ANN models are needed to more precisely capture  
829 the neural mechanisms underlying primate object vision.

830

831 With regards to new ANN models, we can attempt to make prospective inferences about  
832 future possible DCNN<sub>IC</sub> models from the data presented here. Based on the observed distribution  
833 of image-level *human-consistency* values for the DCNN<sub>IC</sub> models tested here, we infer that yet  
834 untested model instances sampled identically (i.e. from the DCNN<sub>IC</sub> model sub-family) are very  
835 likely to have similarly inadequate image-level *human-consistency*. While we cannot rule out the  
836 possibility that at least one model instance within the DCNN<sub>IC</sub> sub-family would fully match the  
837 image-level behavioral signatures, the probability of sampling such a model is vanishingly small  
838 ( $p < 10^{-17}$  for B.I2n *human-consistency*, estimated using exact test using Gaussian kernel density  
839 estimation, see Methods, Results). An important caveat of this inference is that we may have a  
840 biased estimate of the *human-consistency* distribution of this model sub-family, as we did not  
841 exhaustively sample the sub-family. In particular, if the model sampling process is non-  
842 stationary over time (e.g. increases in computational power over time allows larger models to be  
843 successfully trained), the *human-consistency* of new (i.e. yet to be sampled) models may lie  
844 outside the currently estimated distribution. Consistent with the latter, we observed that current  
845 DCNN<sub>IC</sub> cluster into two distinct “generations” separated in time (before/after the year 2015; e.g.  
846 Inception-v3 improves over AlexNet though both lie outside the primate zone in Figure 3). Thus,  
847 following this trend, it is possible that the evolution of “next-generation” models within the  
848 DCNN<sub>IC</sub> sub-family could meet our criteria for successful matching primate-like behavior.

849

850 Alternatively, it is possible—and we think likely—that future DCNN<sub>IC</sub> models will also  
851 fail to capture primate-like image-level behavior, suggesting that either the architectural  
852 limitations (e.g. convolutional, feed-forward) and/or the optimization procedure (including the  
853 diet of visual images) that define this model sub-family are fundamentally limiting. Thus, ANN  
854 model sub-families utilizing different architectures (e.g. recurrent neural networks) and/or  
855 optimized for different behavioral goals (e.g. loss functions other than object classification  
856 performance, and/or images other than category-labeled ImageNet images) may be necessary to

857 accurately capture primate behavior. To this end, we propose that testing even individual  
858 changes to the DCNN<sub>IC</sub> models—each creating a new ANN model sub-family—may be the best  
859 way forward, because DCNN<sub>IC</sub> models currently offer the best explanations (in a predictive  
860 sense) of both the behavioral and neural phenomena of core object recognition.

861

862 To reach that goal of finding a new ANN model sub-family that is a better mechanistic  
863 model of the primate ventral visual stream, we propose that even larger-scale, high-resolution  
864 behavioral measurements, such as expanded versions of the patterns of image-level performance  
865 presented here, could serve as a useful top-down optimization guides. Not only do these high-  
866 resolution behavioral signatures have the statistical power to reject the currently leading ANN  
867 models, but they can also be efficiently collected at very large scale, in contrast to other guide  
868 data (e.g. large-scale neuronal measurements). Indeed, current technological tools for high-  
869 throughput psychophysics in humans and monkeys (e.g. Amazon Mechanical Turk for humans,  
870 Monkey Turk for rhesus monkeys) enable time- and cost-efficient collection of large-scale  
871 behavioral datasets, such as the ~1 million behavioral trials obtained for the current work. These  
872 systems trade off an increase in efficiency with a decrease in experimental control. For example,  
873 we did not impose experimental constraints on subjects' acuity and we can only infer likely head  
874 and gaze position. Previous work has shown that patterns of behavioral performance on object  
875 recognition tasks from in-lab and online subjects were equally reliable and virtually identical  
876 (Majaj et al., 2015), but it is not yet clear to what extent this holds at the resolution of individual  
877 images, as one might expect that variance in performance across images is more sensitive to  
878 precise head and gaze location. For this reason, we here refrain from making strong inferences  
879 from small behavioral differences, such as the small difference between humans and monkeys.  
880 Nevertheless, we argue that this sacrifice in exact experimental control while retaining sufficient  
881 power for model comparison is a good tradeoff for efficiently collecting large behavioral datasets  
882 toward the goal of constraining future models of the primate ventral visual stream.

883

884 **REFERENCES**

885  
886 Cadena SA, Denfield GH, Walker EY, Gatys LA, Tolias AS, Bethge M, Ecker AS (2017) Deep  
887 convolutional models improve predictions of macaque V1 responses to natural images.  
888 bioRxiv:201764.  
889 Cadieu CF, Hong H, Yamins DL, Pinto N, Ardila D, Solomon EA, Majaj NJ, DiCarlo JJ (2014)  
890 Deep neural networks rival the representation of primate IT cortex for core visual object  
891 recognition. PLoS computational biology 10:e1003963.  
892 Cichy RM, Khosla A, Pantazis D, Torralba A, Oliva A (2016) Comparison of deep neural  
893 networks to spatio-temporal cortical dynamics of human visual object recognition reveals  
894 hierarchical correspondence. Scientific reports 6:27755.  
895 DiCarlo JJ, Johnson KO (1999) Velocity invariance of receptive field structure in somatosensory  
896 cortical area 3b of the alert monkey. Journal of Neuroscience 19:401-419.  
897 DiCarlo JJ, Cox DD (2007) Untangling invariant object recognition. Trends in cognitive sciences  
898 11:333-341.  
899 DiCarlo JJ, Zoccolan D, Rust NC (2012) How does the brain solve visual object recognition?  
900 Neuron 73:415-434.  
901 Dodge S, Karam L (2017) A Study and Comparison of Human and Deep Learning Recognition  
902 Performance Under Visual Distortions. arXiv preprint arXiv:170502498.  
903 Geirhos R, Janssen DH, Schütt HH, Rauber J, Bethge M, Wichmann FA (2017) Comparing  
904 deep neural networks against humans: object recognition when the signal gets weaker. arXiv  
905 preprint arXiv:170606969.  
906 Goodfellow IJ, Shlens J, Szegedy C (2014) Explaining and harnessing adversarial examples.  
907 arXiv preprint arXiv:14126572.  
908 Güçlü U, van Gerven MA (2015) Deep neural networks reveal a gradient in the complexity of  
909 neural representations across the ventral stream. Journal of Neuroscience 35:10005-10014.  
910 He K, Zhang X, Ren S, Sun J (2016) Deep residual learning for image recognition. In:  
911 Proceedings of the IEEE conference on computer vision and pattern recognition, pp 770-778.  
912 Hong H, Yamins DL, Majaj NJ, DiCarlo JJ (2016) Explicit information for category-orthogonal  
913 object properties increases along the ventral stream. Nature neuroscience 19:613.  
914 Hosseini H, Xiao B, Jaiswal M, Poovendran R (2017) On the Limitation of Convolutional Neural  
915 Networks in Recognizing Negative Images. human performance 4:6.  
916 Huynh DQ (2009) Metrics for 3D rotations: Comparison and analysis. Journal of Mathematical  
917 Imaging and Vision 35:155-164.  
918 Johnson KO, Hsiao SS, Yoshioka T (2002) Neural coding and the basic law of psychophysics.  
919 The Neuroscientist 8:111-121.  
920 Jozwik KM, Kriegeskorte N, Mur M (2016) Visual features as stepping stones toward semantics:  
921 Explaining object similarity in IT and perception with non-negative least squares.  
922 Neuropsychologia 83:201-226.  
923 Khaligh-Razavi S-M, Kriegeskorte N (2014) Deep supervised, but not unsupervised, models  
924 may explain IT cortical representation. PLoS computational biology 10:e1003915.  
925 Kheradpisheh SR, Ghodrati M, Ganjtabesh M, Masquelier T (2016) Deep networks can  
926 resemble human feed-forward vision in invariant object recognition. Scientific reports 6:32672.  
927 Krizhevsky A, Sutskever I, Hinton GE (2012) Imagenet classification with deep convolutional  
928 neural networks. In: Advances in neural information processing systems, pp 1097-1105.  
929 Kubilius J, Bracci S, de Beeck HPO (2016) Deep neural networks as a computational model for  
930 human shape sensitivity. PLoS computational biology 12:e1004896.  
931 LeCun Y, Bengio Y, Hinton G (2015) Deep learning. Nature 521:436-444.

932 Majaj NJ, Hong H, Solomon EA, DiCarlo JJ (2015) Simple Learned Weighted Sums of Inferior  
933 Temporal Neuronal Firing Rates Accurately Predict Human Core Object Recognition  
934 Performance. *The Journal of Neuroscience* 35:13402-13418.

935 Nguyen A, Yosinski J, Clune J (2015) Deep neural networks are easily fooled: High confidence  
936 predictions for unrecognizable images. In: *Proceedings of the IEEE Conference on Computer*  
937 *Vision and Pattern Recognition*, pp 427-436.

938 Peterson JC, Abbott JT, Griffiths TL (2016) Adapting deep network features to capture  
939 psychological representations. *arXiv preprint arXiv:160802164*.

940 Pinto N, Cox DD, DiCarlo JJ (2008) Why is real-world visual object recognition hard? *PLoS*  
941 *computational biology* 4:e27.

942 Rajalingham R, Schmidt K, DiCarlo JJ (2015) Comparison of Object Recognition Behavior in  
943 Human and Monkey. *The Journal of Neuroscience* 35:12127-12136.

944 RichardWebster B, Anthony SE, Scheirer WJ (2016) PsyPhy: A Psychophysics Driven  
945 Evaluation Framework for Visual Recognition. *arXiv preprint arXiv:161106448*.

946 Rosch E, Mervis CB, Gray WD, Johnson DM, Boyes-Braem P (1976) Basic objects in natural  
947 categories. *Cognitive psychology* 8:382-439.

948 Seibert D, Yamins DL, Ardila D, Hong H, DiCarlo JJ, Gardner JL (2016) A performance-  
949 optimized model of neural responses across the ventral visual stream. *bioRxiv:036475*.

950 Simonyan K, Zisserman A (2014) Very deep convolutional networks for large-scale image  
951 recognition. *arXiv preprint arXiv:14091556*.

952 Szegedy C, Zaremba W, Sutskever I, Bruna J, Erhan D, Goodfellow I, Fergus R (2013)  
953 Intriguing properties of neural networks. *arXiv preprint arXiv:13126199*.

954 Ullman S, Humphreys GW (1996) High-level vision: Object recognition and visual cognition: MIT  
955 press Cambridge, MA.

956 Wallis TS, Funke CM, Ecker AS, Gatys LA, Wichmann FA, Bethge M (2017) A parametric  
957 texture model based on deep convolutional features closely matches texture appearance for  
958 humans. *Journal of vision* 17:5-5.

959 Wen H, Shi J, Zhang Y, Lu K-H, Cao J, Liu Z (2017) Neural encoding and decoding with deep  
960 learning for dynamic natural vision. *Cerebral Cortex*:1-25.

961 Yamins DL, DiCarlo JJ (2016) Using goal-driven deep learning models to understand sensory  
962 cortex. *Nature neuroscience* 19:356-365.

963 Yamins DL, Hong H, Cadieu C, DiCarlo JJ (2013) Hierarchical modular optimization of  
964 convolutional networks achieves representations similar to macaque IT and human ventral  
965 stream. In: *Advances in neural information processing systems*, pp 3093-3101.

966 Yamins DL, Hong H, Cadieu CF, Solomon EA, Seibert D, DiCarlo JJ (2014) Performance-  
967 optimized hierarchical models predict neural responses in higher visual cortex. *Proceedings of*  
968 *the National Academy of Sciences*:201403112.

969 Zeiler MD, Fergus R (2014) Visualizing and understanding convolutional networks. In: *Computer*  
970 *Vision–ECCV 2014*, pp 818-833: Springer.

971

972

973 **TABLES**

974 **Table 1**

Behavioral Metric	Hit Rate	False Alarm Rate
One-versus all object-level performance (B.O1) ( $N_{\text{objects}} \times 1$ ) $O_1(i) = Z(HR(i)) - Z(FAR(i)),$ $i = 1, 2, \dots, N_{\text{objects}}$	Proportion of trials when images of object $i$ were correctly labeled as object $i$ .	Proportion of trials when any image was incorrectly labeled as object $i$ .
One-versus-other object-level performance B.O2 ( $N_{\text{objects}} \times N_{\text{objects}}$ ) $O_2(i, j) = Z(HR(i, j)) - Z(FAR(i, j)),$ $i = 1, 2, \dots, N_{\text{objects}}$ $j = 1, 2, \dots, N_{\text{objects}}$	Proportion of trials when images of object $i$ were correctly labeled as $i$ , when presented against distractor object $j$ .	Proportion of trials when images of object $j$ were incorrectly labeled as object $i$
One-versus-all image-level performance B.I1 ( $N_{\text{images}} \times 1$ ) $I_1(ii) = Z(HR(ii)) - Z(FAR(ii)),$ $ii = 1, 2, \dots, N_{\text{images}}$	Proportion of trials when image $ii$ was correctly classified as object $i$ .	Proportion of trials when any image was incorrectly labeled as object $i$ .
One-versus-other image-level performance B.I2 ( $N_{\text{images}} \times N_{\text{objects}}$ ) $I_2(ii, j) = Z(HR(ii, j)) - Z(FAR(ii, j)),$ $ii = 1, 2, \dots, N_{\text{images}}$ $j = 1, 2, \dots, N_{\text{objects}}$	Proportion of trials when image $ii$ was correctly classified as object $i$ , when presented against distractor object $j$ .	Proportion of trials when images of object $j$ were incorrectly labeled as object $i$

975

976 **Table 1: Definition of behavioral performance metrics.** The first column provides the name,  
977 abbreviation, dimensions, and equations for each of the raw performance metrics. The next two  
978 columns provide the definitions for computing the hit rate (HR) and false alarm rate (FAR)  
979 respectively.

980

981 **FIGURE LEGENDS**

982

983 **Figure 1. Images and behavioral task.** **(A)** Two (out of 100) example images for each of the 24  
984 basic-level objects. To enforce true invariant object recognition behavior, we generated  
985 naturalistic synthetic images, each with one foreground object, by rendering a 3D model of each  
986 object with randomly chosen viewing parameters and placing that foreground object view onto a  
987 randomly chosen, natural image background. **(B)** Time course of example behavioral trial (zebra  
988 versus dog) for human psychophysics. Each trial initiated with a central fixation point for 500  
989 ms, followed by 100 ms presentation of a square test image (spanning 6-8° of visual angle).  
990 After extinction of the test image, two choice images were shown to the left and right. Human  
991 participants were allowed to freely view the response images for up to 1000 ms and responded  
992 by clicking on one of the choice images; no feedback was given. To neutralize top-down feature  
993 attention, all 276 binary object discrimination tasks were randomly interleaved on a trial-by-trial  
994 basis. The monkey task paradigm was nearly identical to the human paradigm, with the  
995 exception that trials were initiated by touching a fixation circle horizontally centered on the  
996 bottom third of the screen, and successful trials were rewarded with juice while incorrect choices  
997 resulted in timeouts of 1–2.5s. **(C)** Large-scale and high-throughput psychophysics in humans  
998 (top left), monkeys (top right), and models (bottom). Human behavior was measured using the  
999 online Amazon MTurk platform, which enabled the rapid collection ~1 million behavioral trials  
1000 from 1472 human subjects. Monkey behavior was measured using a novel custom home-cage  
1001 behavioral system (MonkeyTurk), which leveraged a web-based behavioral task running on a  
1002 tablet to test many monkey subjects simultaneously in their home environment. Deep  
1003 convolutional neural network models were tested on the same images and tasks as those  
1004 presented to humans and monkeys by extracting features from the penultimate layer of each  
1005 visual system model and training back-end multi-class logistic regression classifiers. All  
1006 behavioral predictions of each visual system model were for images that were not seen in any  
1007 phase of model training.

1008 **Figure 2. Object-level comparison to human behavior.** **(A)** One-versus-all object-level (B.O1)  
1009 signatures for the pooled human (n=1472 human subjects), pooled monkey (n=5 monkey  
1010 subjects), and several DCNN<sub>IC</sub> models. Each B.O1 signature is shown as a 24-dimensional  
1011 vector using a color scale; each colored bin corresponds to the system's discriminability of one

1012 object against all others that were tested. The color scales span each signature's full performance  
1013 range, and warm colors indicate lower discriminability. **(B)** Direct comparison of the B.O1  
1014 signatures of a pixel visual system model (top panel) and a DCNN<sub>IC</sub> visual system model  
1015 (Inception-v3, bottom panel) against that of the human B.O1 signature. **(C)** *Human-consistency*  
1016 of B.O1 signatures, for each of the tested model visual systems. The black and gray dots  
1017 correspond to a held-out pool of five human subjects and a pool of five macaque monkey  
1018 subjects respectively. The shaded area corresponds to the “primate zone,” a range of  
1019 consistencies delimited by the estimated *human-consistency* of a pool of infinitely many  
1020 monkeys (see Figure 4A). **(D)** One-versus-other object-level (B.O2) signatures for pooled  
1021 human, pooled monkey, and several DCNN<sub>IC</sub> models. Each B.O2 signature is shown as a 24x24  
1022 symmetric matrices using a color scale, where each bin  $(i,j)$  corresponds to the system's  
1023 discriminability of objects  $i$  and  $j$ . Color scales similar to (A). **(E)** Human-consistency of B.O2  
1024 signatures for each of the tested model visual systems. Format is identical to (C).

1025 **Figure 3. Image-level comparison to human behavior.** **(A)** Schematic for computing B.I1n.  
1026 First, the one-versus-all image-level signature (B.I1) is shown as a 240-dimensional vector (24  
1027 objects, 10 images/object) using a color scale, where each colored bin corresponds to the  
1028 system's discriminability of one image against all distractor objects. From this pattern, the  
1029 normalized one-versus-all image-level signature (B.I1n) is estimated by subtracting the mean  
1030 performance value over all images of the same object. This normalization procedure isolates  
1031 behavioral variance that is specifically image-driven but not simply predicted by the object. **(B)**  
1032 Normalized one-versus-all object-level (B.I1n) signatures for the pooled human, pooled monkey,  
1033 and several DCNN<sub>IC</sub> models. Each B.I1n signature is shown as a 240-dimensional vector using a  
1034 color scale, formatted as in (A). Color scales similar to Figure 2A. **(C)** *Human-consistency* of  
1035 B.I1n signatures for each of the tested model visual systems. Format is identical to Figure 2C.  
1036 **(D)** Normalized one-versus-other image-level (B.I2n) signatures for pooled human, pooled  
1037 monkey, and several DCNN<sub>IC</sub> models. Each B.I2n signature is shown as a 240x24 matrix using a  
1038 color scale, where each bin  $(i,j)$  corresponds to the system's discriminability of image  $i$  against  
1039 distractor object  $j$ . Color scales similar to Figure 2A. **(E)** Human-consistency of B.I2n signatures  
1040 for each of the tested model visual systems. Format is identical to Figure 2C.

1041 **Figure 4. Effect of subject pool size and DCNN model modifications on consistency with**  
1042 **human behavior.** **(A)** Accounting for natural subject-to-subject variability. For each of the four  
1043 behavioral metrics, the *human-consistency* distributions of monkey (blue markers) and model  
1044 (black markers) pools are shown as a function of the number of subjects in the pool (mean  $\pm$  SD,  
1045 over subjects). The human consistency increases with growing number of subjects for all visual  
1046 systems across all behavioral metrics. The dashed lines correspond to fitted exponential  
1047 functions, and the parameter estimate (mean  $\pm$  SE) of the asymptotic value, corresponding to the  
1048 estimated *human-consistency* of a pool of infinitely many subjects, is shown at the right most  
1049 point on each abscissa. **(B)** Model modifications that aim to rescue the DCNN<sub>IC</sub> models. We  
1050 tested several simple modifications (see Methods) to the most *human-consistent* DCNN<sub>IC</sub> visual  
1051 system model (Inception-v3). Each panel shows the resulting *human-consistency* per modified  
1052 model (mean  $\pm$  SD over different model instances, varying in random filter initializations) for  
1053 each of the four behavioral metrics.

1054

1055 **Figure 5. Analysis of unexplained human behavioral variance.** **(A)** Residual similarity  
1056 between all pairs of human visual system models. The color of bin  $(i,j)$  indicates the proportion  
1057 of explainable variance that is shared between the residual signatures of visual systems  $i$  and  $j$ .  
1058 For ease of interpretation, we ordered visual system models based on their architecture and  
1059 optimization procedure and partitioned this matrix into four distinct regions. **(B)** Summary of  
1060 residual similarity. For each of the four regions in Figure 5A, the similarity to the residuals of  
1061 Inception-v3 (region 2 in (A)) is shown (mean  $\pm$  SD, within each region) for all images (black  
1062 dots), and for images that humans found to be particularly difficult (gray dots, selected based on  
1063 held-out human data).

1064

1065 **Figure 6. Dependence of primate and DCNN model behavior on image attributes.** **(A)**  
1066 Example images with increasing attribute value, for each of the four pre-defined image attributes  
1067 (see Methods). **(B)** Dependence of performance (B.I1n) as a function of four image attributes, for  
1068 humans, monkeys and a DCNN<sub>IC</sub> model (Inception-v3). **(C)** Proportion of explainable variance  
1069 of the residual signatures of monkeys (black) and DCNN<sub>IC</sub> models (blue) that is accounted for by  
1070 each of the pre-defined image attributes. Error-bars correspond to SD over trial re-sampling for  
1071 monkeys, and over different models for DCNN<sub>IC</sub> models.

Figure 1

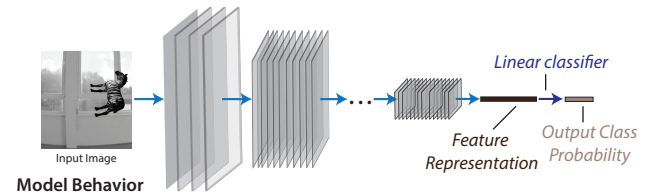
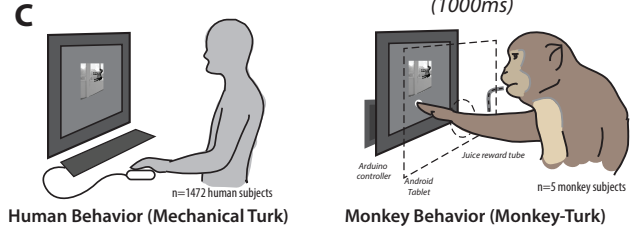
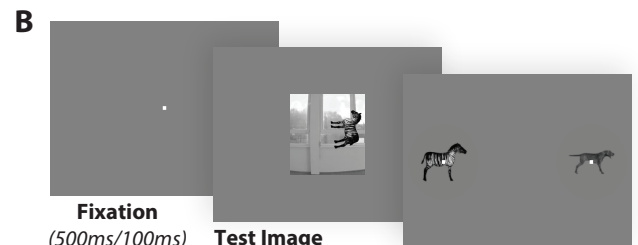
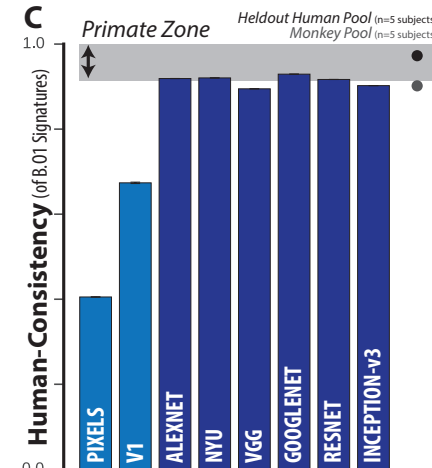
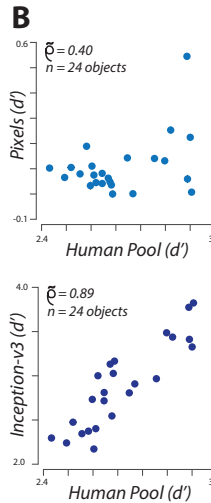
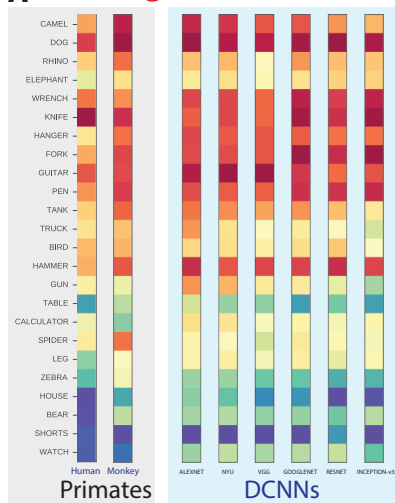
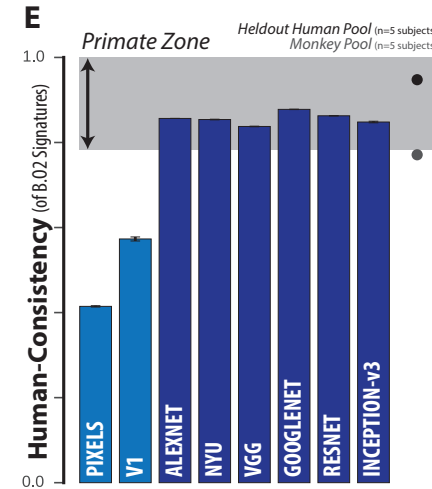
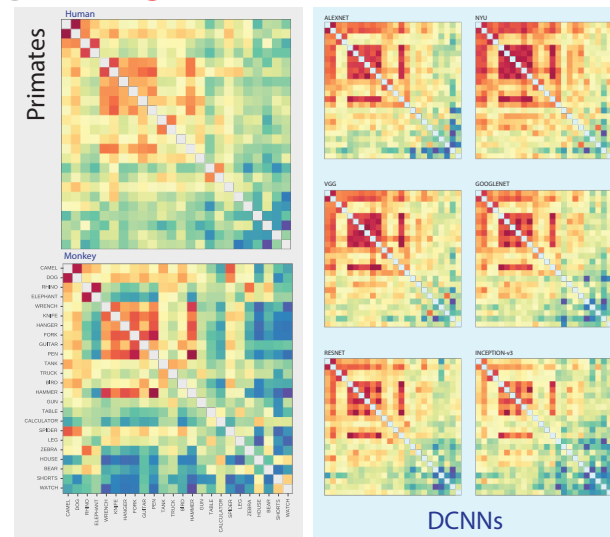


Figure 2

**A B.O1 Signatures (~object difficulties)****D B.O2 Signatures (~object confusions)**

**Figure 3****A B.I1n Signatures** (~normalized image difficulties)

10 images/object

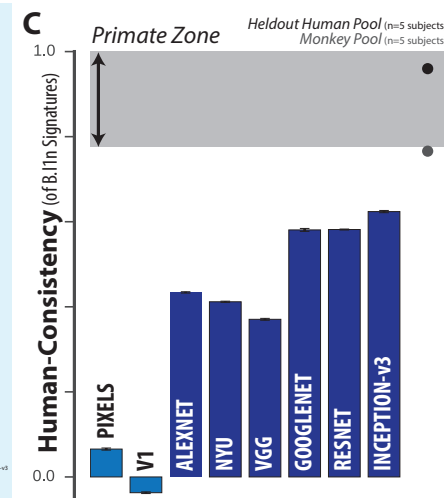
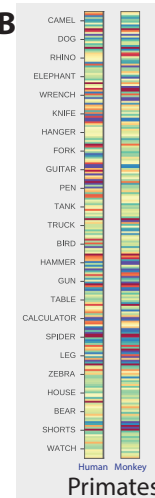
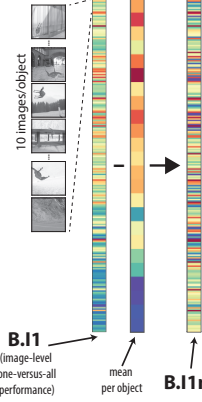
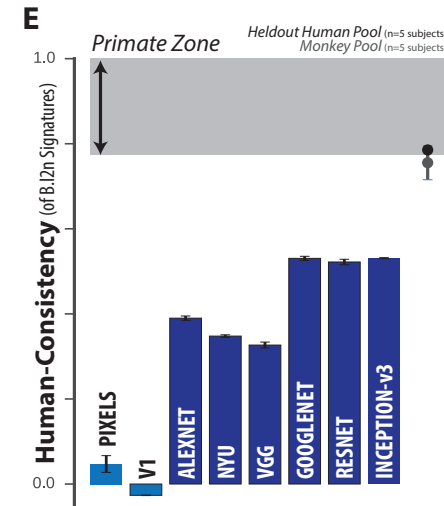
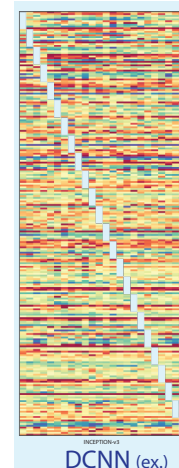
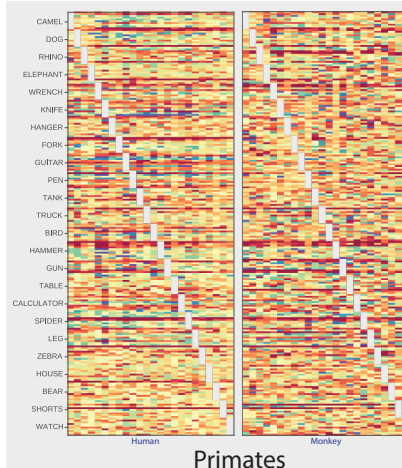
**D B.I2n Signatures** (~normalized image confusions)

Figure 4

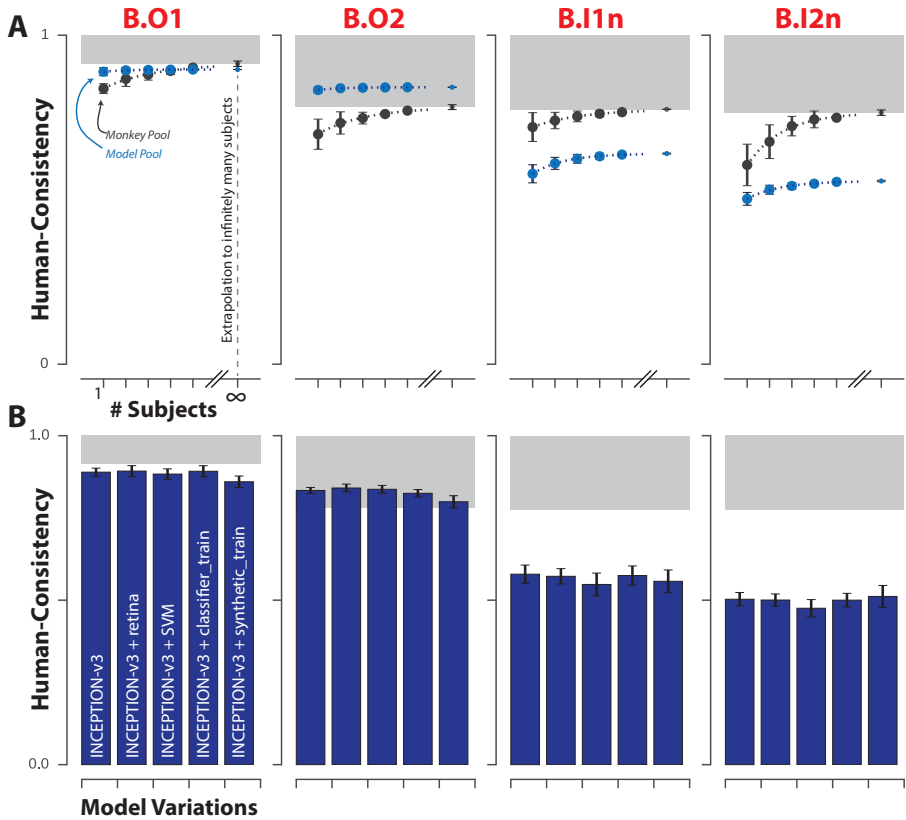
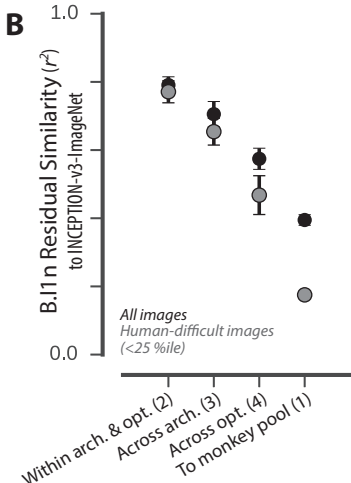
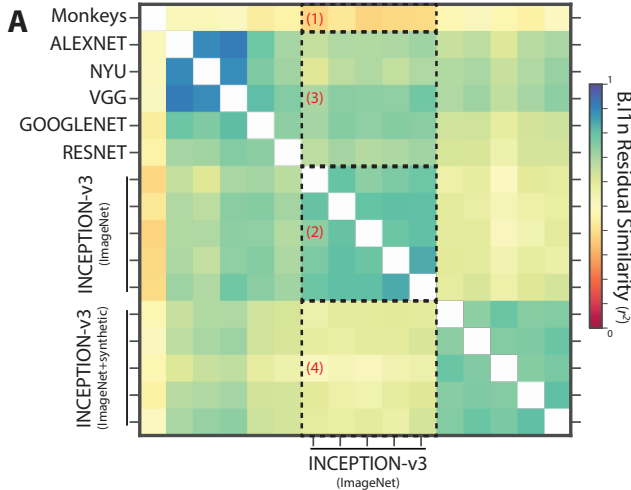


Figure 5



# Figure 6

